Real-time Optimal Planning and Adaptive Sampling for Multi-Platform Operations in the Gulf of Mexico

C. Mirabito[a], P. J. Haley, Jr.[a], E. M. Mule[a], A. V. Rodriguez[a], S. L. Morey[b], E. P. Chassignet[c], S. M. Glenn[d], T. N. Miles[d], D. Aragon[d], K. Coleman[d], M. Smith[d], S. F. DiMarco[e], S. Mahmud[e], X. Ge[e], A. H. Knap[e], B. Jaimes de la Cruz[f], L. K. Shay[f], M. Leber[g], R. Ramos[g], H. Nowak[g], J. Storie[g], A. Romer[g], M. Tenreiro[h], E. Pallàs-Sanz[h], J. Sheinbaum[h], P. Pérez-Brunius[h], R. He[i], Y. Deng[i], T. Wu[i], A. Bower[j], H. H. Furey[j], K. A. Donohue[k], J. van Smirren[l], P. Hogan[m,n], G. Jacobs[m], M. Feldman[o], F. K. Wiese[o], M. Khadka[o], P. F. J. Lermusiaux[a,†]

[a]*Massachusetts Institute of Technology* [b]*Florida A&M Univ.* [c]*Florida State Univ.* [d]*Rutgers Univ.* [e]*Texas A&M Univ.*
[f]*Univ. of Miami* [g]*CICESE* [h]*Woods Hole Group, Inc.* [i]*North Carolina State Univ.*
[j]*Woods Hole Oceanographic Institute* [k]*Univ. of Rhode Island* [l]*Ocean Sierra* [m]*NRL* [n]*NOAA* [o]*NASEM*
[†]Corresponding author: pierrel@mit.edu

***Abstract*—In this paper, we use our MIT Multidisciplinary Simulation, Estimation, and Assimilation Systems (MSEAS) including Error Subspace Statistical Estimation (ESSE) large-ensemble forecasting to provide real-time probabilistic forecasts for the Gulf of Mexico during the collaborative GRand Adaptive Sampling Experiment (GRASE) from April to September 2025. These forecasts are used for optimal planning and adaptive sampling for multiple platforms deployed during the experiment. We highlight real-time forecasts for probabilistic glider reachability and optimal planning. We showcase mutual information forecasts for optimal adaptive sampling with gliders and floats, maximizing information about the Loop Current (LC) and its eddies (LCEs). We showcase reachability and flow map forecasts for floats, characterizing water mass transports and eddy filamentations. We present probabilistic LCE forecasts using clustering techniques. Finally, we guide two gliders to recovery points using reachability and heading forecasts.**

***Index Terms*—Ocean forecasting, sea glider, floats, path planning, reachability analysis, probabilistic forecasting, mutual information, adaptive sampling, Loop Current System.**

I. Introduction

Real-time planning for multi-platform operations in the Gulf of Mexico (GoM) is a critical element of successful ocean campaigns. Such quantitative planning is useful for the optimal deployment, coordination, and recovery of multiple assets, as well as for improved exploration, monitoring, understanding, and even long-term forecasting. The GRand Adaptive Sampling Experiment (GRASE) is a collaborative sea experiment that occurs in the GoM from April to September 2025. It is a key component of the "Understanding Gulf Ocean Systems (UGOS-3)" initiative sponsored by the Gulf Research Program of the U.S. National Academies of Sciences, Engineering, and Medicine. The main goals of GRASE are to "assess the impact of observations within cyclonic features of the [Loop Current System (LCS), namely cyclonic Loop Current Frontal Eddies (LCFEs),] obtained through adaptive sampling on the prediction skill of forecast systems; and provide a framework to improve confidence in and validate the numerical models' ability to properly represent [Loop Current (LC)] evolution and eddy shedding events [e.g., separation of LC eddies, LCEs], including the distribution and paths of the cyclonic eddies that have been shown to be essential in the separation process."

The Loop Current (LC) system, along with its meanders and eddies, plays a major role in the GoM and has consequently been the subject of intense study over the past decade [1–16], with several field campaigns [17, 18]. For more on the LC and its dynamics, we refer to these manuscripts and references therein. For real-time coordinated sampling and forecasting in the GoM, we also refer to the recent MASTR experiment [19, 20], a precursor to GRASE. Recent developments include studies of cyclonic eddies in the LCE separation process [21], ensemble hindcasts to predict LCE separation [22], machine learning to identify and predict Lagrangian coherent eddies [23], as well as eddy spiraling and filamentation [24].

During the 6-month GRASE observation period, we employed our MSEAS Primitive-Equation (PE) submesoscale-to-regional-scale ocean modeling system [20, 25–28], processed multiple data types, and issued deterministic and probabilistic forecasts of ocean fields and derived quantities in real time. We provided (i) large-ensemble forecasts with initial conditions downscaled from HYCOM, four-regions 3D PE-field perturbations using Error Subspace Statistical Estimation (ESSE), and stochastic tidal and atmospheric forcing; (ii) hazardous velocities statistics, a key metric for the GoM industry and platform operators; and (iii) deterministic and probabilistic reachability forecasts for underwater vehicles, including time-optimal paths and vehicle headings. We also issued mutual information (MI) forecasts for optimal adaptive sampling with gliders and floats [29, 30] aiming to maximize information about the LC, LCEs, and LCFEs; Lagrangian flow maps forecasts [31–33] to characterize water mass transports and eddy filamentations, and several reachability and modified-Lagrangian forecasts for float planning products, accounting for different parking depths and vertical profiling.

In this paper, we present some of the above real-time GRASE results, building upon our prior 2024 Mini-Adaptive Sampling Test Run (MASTR) experiment [20, 34]. In Sec. II, we outline our probabilistic ocean modeling system, including the forecast skill assessment, Lagrangian flow maps, reachability and path planning forecasting systems, and adaptive sampling methodology. In Sec. III, we overview our real-time

efforts. In Sec. IV, we highlight several optimal glider planning forecasts. Sec. V showcases optimal adaptive sampling guidance for multiple sensing platforms. Sec. VI highlights our optimal float deployment planning products, while Sec. VII contains likelihood forecasts of LCEs separation. In Sec. VIII, we illustrate real-time products for glider recovery requests. Finally, we conclude in section IX.

II. Forecasting Methodology and Setup

a) Ocean Forecasting Overview and Setup: We used our MIT MSEAS modeling systems [25, 26, 35–38] to provide large-ensemble forecasts of physical ocean fields and uncertainties; all our other forecast products used outputs from these systems (e.g., Fig. 1). They have been used for many regional ocean simulations [30, 32, 39–43]. They can simulate submesoscale processes over domains with complex geometries using an implicit two-way nesting/tiling scheme [25]. During GRASE, we leveraged many of our systems' capabilities, including deterministic and ensemble initialization schemes [26, 44, 45], tidal prediction and inversion [46], fast-marching coastal objective analysis [47], subgrid-scale models [48, 49], and path planning, reachability and adaptive sampling [30, 50–52]. Forecasts of 5-to-20-day duration were issued several times per week, using 100 optimized vertical levels and 1/25° horizontal resolution over the GoM and western Caribbean. Initial conditions were downscaled from HYCOM and data-corrected. Tidal forcing was based on OSU's TPXO10-Atlas, adapted to high-resolution bathymetry and coastlines [46]. The sources of atmospheric forcing and bathymetry were the same as for the MASTR experiment (see [20]). GRASE data and data of opportunity (Argo float, glider CTDs, float positions, satellite SSH/SST/SSC, etc.) were processed and used to evaluate forecasts [53].

b) Ensemble Methodology and Setup: Our large ESSE ensemble forecasts are initialized [49, 52, 54] with perturbed ICs/BCs and stochastic forcing [27, 29, 49, 55]. The setup procedure for creating 3D PE-balanced initial ESSE perturbations using 3D temperature and salinity modes [27, 44, 45] is described in [20], and remains largely the same here. The ESSE ensembles are forced with stochastic boundary, tidal, and atmospheric forcing. We provided real-time probabilistic forecasts of the locations of surface currents exceeding 1.5 kt as such velocities can be hazardous for the GoM industry (e.g., Fig. 1e). Lastly, we predicted event and feature statistics using clustering techniques, where we partition ensemble realizations into groups (clusters) depending on event types. For example, we clustered SSH contours of our ensembles to forecast the probability of LCE separations (see Sec. VII).

c) Forecast Skill: We compared our forecasts with independent data in a variety of ways [53]. This includes horizontal maps of predicted T/S against profile data at different depths (see Fig. 1h) and predicted velocity against that measured by gliders (see Sec. IV). Other forecast skill products we utilized include (i) feature skill assessment, comparing forecast SSH, SST, and SSC against the LC and eddy shapes and locations given by satellite data and other models (e.g., CMEMS, ESPC, and RTOFS); (ii) comparisons of forecast T/S against that from Argo float and glider profiles; and (iii) comparisons of forecast T/S against that from glider vertical sections.

d) Lagrangian Flowmaps and Transports: To describe water mass transports and eddy filamentations, we used our Lagrangian forward/backward flow maps: they display, at the initial/final location of a water parcel, the final/initial position of that parcel as it is advected over a specified time window. We modify these pure-advection functions for floats by accounting for the vertical profiling motions [56]. Flowmaps are computed using our PDE-based method of composition [31], extended for use in realistic open-flow fields, with time-dependent inlets and outlets. They have been successfully used to forecast water mass transport in several regions (see [33]).

e) Reachability and Path Planning: We used our path planning software to compute reachability fronts, time-optimal paths, and optimal headings. A reachability front is the boundary of the largest set (the reachable set) that a platform (glider, float, AUV, etc.) can reach within that duration. It is computed by numerically solving the exact PDE governing reachability sets [30, 57–61]. Probabilistic reachable maps are forecasts of the probability that a platform can reach points in a domain at a future time, given the uncertainty in future ocean currents (our ensemble forecasts). To account for vertical glider motions, we use our forecast velocities averaged over the dive depth; for floats, we construct a velocity field based on the float's daily vertical profiling motions and parking depth.

f) Adaptive Sampling: For targeted observations [51, 52], we use mutual information (MI) forecasts between candidate observation locations and future regional field or variables of interest (target or verification field/variables) and predict the most informative future data locations [20, 27, 30]. We use our ensemble forecasts to compute and predict these MI fields.

III. Overview of MSEAS Real-time Forecasting

Figure 1 illustrates a selection of our real-time results and products [53]. Fig. 1(a) is a forecast of deterministic glider reachability fronts for May 12–22, 2025 (black contours, increasing line thickness for later times), starting from the position of glider RU38 at 1520Z on May 12 and assuming a glider speed of 30 cm/s. A reachability front is the boundary of the largest set that a glider can reach within a given duration, and is computed using exact governing equations and high-order level-set schemes [30, 57]. The red lines denote EEZ boundaries. We also issued reachability forecasts for different glider speeds, as well as time-optimal paths and headings for different targets such as Tortugas eddies, western branch of the LC, or specific pick-up locations. To account for uncertainty in our forecast currents and provide probabilistic field and reachability forecasts, we issued ESSE ensemble forecasts. Fig. 1(b) illustrates one of such products, a 6-day forecast of glider reachability probability for May 19. Fig. 1(c) showcases a forecast of 150 m salinity for May 18. This is the depth around which subsurface salinity maxima occur for modified subtropical Caribbean waters that cross the Yucatan Channel. Such maxima were confirmed by Argo and glider

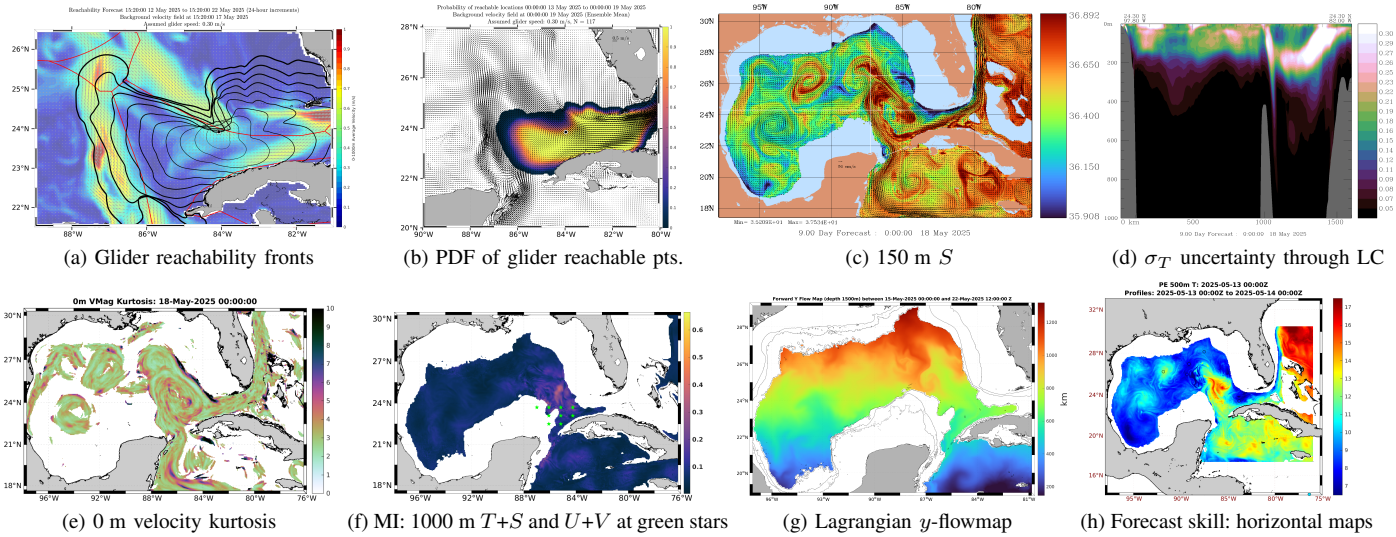

(a) Glider reachability fronts (b) PDF of glider reachable pts. (c) 150 m S (d) σ_T uncertainty through LC

(e) 0 m velocity kurtosis (f) MI: 1000 m T+S and U+V at green stars (g) Lagrangian y-flowmap (h) Forecast skill: horizontal maps

Fig. 1: Illustration of MSEAS real-time forecast products issued during GRASE on May 11, 2025 [53]: (a) Deterministic glider reachability front forecasts for 12 to 22 May, (b) Reachability probability on 19 May by a glider starting at the black dot on 13 May, (c) 150 m S forecast for 18 May, capturing filamentation, (d) 0-1000 m vertical section along 24.3°N of ensemble standard deviation (uncertainty) forecast of σ_T for 19 May, crossing the LC as it flows north along Campeche Bank and then southeastward to enter Florida Strait, (e) 0 m velocity kurtosis forecast for May 18, with the highest values near the edges and interior jets of the LC and LCEs, (f) Forecast mutual information (MI) between 1000 m T+S on May 11 and upper layer U+V profiles around the LC neck (green stars) on May 19, (g) Forward y-flowmap forecast between May 15 and May 22, (h) 500 m T forecast compared with Argo float and glider profile values on May 13.

data, and already successfully forecast in 2024 [20]. The forecast shows all the main features (e.g., extended LC, eddy Edison, and two anticyclonic eddies in the western Gulf), and captures filamentation in spiral shapes around the LCEs and LC meanders. These high-salinity filaments were later confirmed by the glider data (not shown). Fig. 1(d) shows a forecast of uncertainty (ensemble standard deviation) for σ_T on May 18, along a vertical section through the inner Gulf and LC neck. The highest uncertainty is seen along the west branch of the LC as well as the branch of the LC exiting through the Florida Strait. Fig. 1(e) is a one-week forecast for May 18 of the surface velocity ensemble kurtosis; the highest values are forecast to be near the edges and interior jets of the LC, eddy Edison, and the two anticyclones in the western Gulf. This product is issued as part of our statistics of surface velocity magnitude that exceeds 1.5 kt and is intended for platform and vehicle operators. In Fig. 1(f), we illustrate a forecast of mutual information (MI) between candidate T and S measurements at 1000 m and velocity fields around the neck of the LC 8 days later. Specifically, we forecast the MI between 1000 m T and S data (together) on May 11 anywhere in the domain and u- and v-velocity (together) on May 19 at a set of nine verification locations (green stars) and three depths (150, 300, and 500 m), hence 27 values of u and v. This MI map thus predicts where 1000 m T and S data should be collected on May 11 to best inform horizontal currents on May 19 in the upper layers of the LC neck. It shows that for this goal, deep T and S data are most useful north of the neck, but also in the anticyclone and LC in the northwest Caribbean Sea. Such forecasts can guide gliders and float releases toward locations most informative about specific future features. In Fig. 1(g), a forecast of the 1500 m Lagrangian forward y-flowmap shows, at the initial time of May 15 0Z, the y-locations of the water parcels at the final time (May 22 12Z). Notice that Caribbean water is advected northward through the Yucatan Channel into the inner Gulf and LC base; northward advection is also seen on the northwest side of the LC. Such forecasts can be used to follow water mass transport in the region. Finally, Fig. 1(h) compares, on May 13, the 4-day forecast 500 m temperature with that measured by floats and gliders. Notice that the overlaid observations (five colored data dots inside black circles) show good agreement with the forecast fields, indicating predictive skill. To refine our modeling system, many forecast skill products were computed and used daily, some of which are on our real-time page [53].

IV. Real-time Probabilistic Reachability and Optimal Planning for Gliders

We illustrate some of our GRASE real-time forecasts for guiding gliders in the Tortugas LCFE, LC neck, and western Caribbean regions from April to July, 2025. All forecasts were issued on our GRASE webpage [53] and WhatsApp for rapid dissemination to glider teams.

Fig. 2 shows one such deterministic reachability forecast for glider RU38 (operated by Rutgers) in late April, and one forecast for glider SG622 (operated by CICESE) in mid-June. In the time-optimal path forecast for glider RU38 (Fig. 2a), we take as start point the glider's reported location of (24.3127°N, 84.6419°W; black dot) on April 24 16:15Z. The final target point (white star) is the center of the Tortugas LCFE as forecast by MSEAS for April 30 0Z. The assumed glider speed is 30 cm/s based on operator guidance. The glider is forecast to use the strong, favorable currents, follow the southwest edge of the LCFE, and reach its target late on April 27 (3 days later). The actual glider track (Fig. 2b) closely resembles our path, and its location after 1, 2, and 3 days is well within

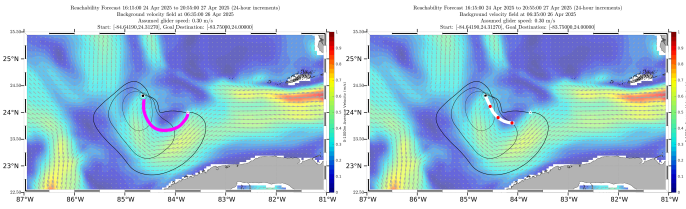

(a) Time-optimal path fct for RU38 (b) RU38 actual track

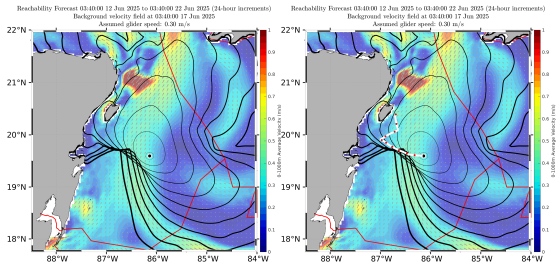

(c) Reachablity fct for SG622 (d) SG622 actual track

Fig. 2: MSEAS deterministic reachability forecasts, with daily reachability fronts (black contours) and paths overlaid on the 0–1000 m average velocity forecasts at the temporal midpoint. (a) 0–3 day time-optimal path forecast (magenta curve) for glider RU38, for April 24–27, targeting the Tortugas LCFE. (b) as (a), but actual glider track (white curve with red dots at daily intervals). (c) 0–10 day forward reachability forecast for glider SG622, for June 12–22. (d) as (c), but actual glider track. Assumed glider speed is 30 cm/s.

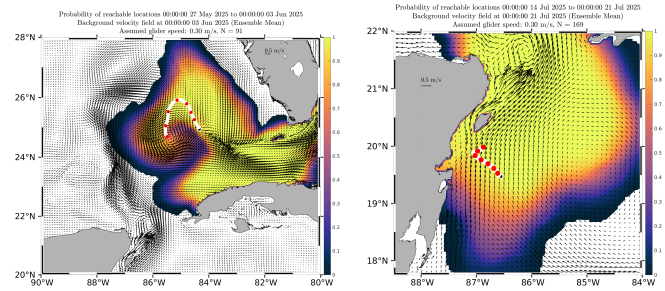

(a) Reachability PDF fct for glider RU38, for June 3 (b) Reachability PDF fct for glider SG622, for July 21

Fig. 3: MSEAS probabilistic reachability forecasts. Assumed glider speed is 30 cm/s. Plots show the probability that the glider can reach anywhere in the colored region by the indicated date from its position 7 days earlier. Yellow regions indicate certain reachability (probability 1); white regions are unreachable (probability 0). Actual glider tracks are overlaid (white curves with red dots at daily intervals).

our corresponding reachability fronts (black curves, shown at 24-hour intervals). The glider position after 3 days is short of the target, however, suggesting a slower actual glider speed than assumed. Similarly, for the 10-day forward reachability forecast for glider SG622 (Fig. 9c–d), which uses the reported position on June 12 03:40Z as the starting point and also assumes a 30 cm/s glider speed per the operator, we see that the glider positions after each day (red dots) all lie within the corresponding reachability sets, as expected. Interestingly, the glider skirts but does not cross the sharp gradients in the forecast fronts, validating this forecast value function.

However, as our ocean forecasts are uncertain, we forecast probabilistic reachability fields from our ESSE ensemble [20, 34]. Fig. 3 shows two such forecasts: one with 91 (Fig. 3a) and the other with 169 members (Fig. 3b), overlaid with ensemble mean velocity vectors at the temporal midpoint of the forecasts. In Fig. 3a, which shows a 7-day forecast of the reachability PDF, starting from the position of glider RU38 on May 27 0Z, the real track proceeds northwest through a region of near-certain reachability, then turns south into the LC near the Tortugas LCFE, avoiding a region with a rapid decay in the PDF. In Fig. 3b, the real track of glider SG622, in the western Caribbean, lies in a region of (much more certain) strong northward currents upstream of the LC, and remains well within our forecast region of near-certain reachability.

Our deterministic forecasts were validated against independent data [53]. For example, in Fig. 4, we compare the 0–1000 m average velocity from the MSEAS-PE forecasts with depth-averaged measurements from the GRASE gliders. These forecasts show relatively good agreement with the data, correctly capturing: southerly and strong southwest currents on the western side of the Tortugas LCFE in late April, and the return flow on the east side of the eddy (Fig. 4a–b); northerly flow at the shelf break and strong southwest currents in the LC in late May (Fig. 4c–d); and strong northward flow in the western Caribbean upstream of the LC in April/May and variability in June (Fig. 4e–h). Over the experiment period, the MSEAS 5-to-12 day forecast 0–1000 m average velocity RMSE was 20 cm/s for glider RU38, 10 cm/s for glider SG622, and 8 cm/s for glider SG651. The higher mean RMSE of glider RU38 is due to the time spent in the strong currents in the LC east branch and Tortugas LCFE edge.

V. Real-time Mutual Information Forecasts for Adaptive Sampling

With each probabilistic forecast, we issued a set of MI fields, where the goal is to predict the locations of candidate future glider and float observations on different days that are the most informative about target ocean features such as the LC, LC neck, LCEs, or LCFEs. Fig. 5 shows one such set of forecasts, for candidate glider T and S profiles at 0 m, 50 m, 150 m, 300 m and 500 m (taken together) on April 30 and a verification (target) feature on May 6, either σ_T or U and V in the LC (green stars on Fig. 5a,b,c,e) or its western side (green stars on Fig. 5d,f). In Fig. 5c,d,e,f), the locations with the highest MI (bright yellow) indicate where the profiles are predicted to be the most informative about the specific LC target on May 6. We find that the upper-layer T/S profiles on April 30 most informative: about σ_T at 50 m, 300 m, and 500 m (together) in the forecast LC head, are near the LC center (Fig. 5c); about σ_T at the western edge of the forecast LC head, are near the southern inflow of the LC (Fig. 5d); about U and V (together) in the forecast LC head, are in an oval shape surrounding the LC at depth, but less in the LC center itself (Fig. 5e); about U and V (together) in the western edge of the forecast LC head, are again at the southern inflow of the LC, but also at the north side of the LC (Fig. 5f).

Fig. 6 shows another set of MI forecasts, focusing on deep candidate observations (1000 m and 1500 m, together) on

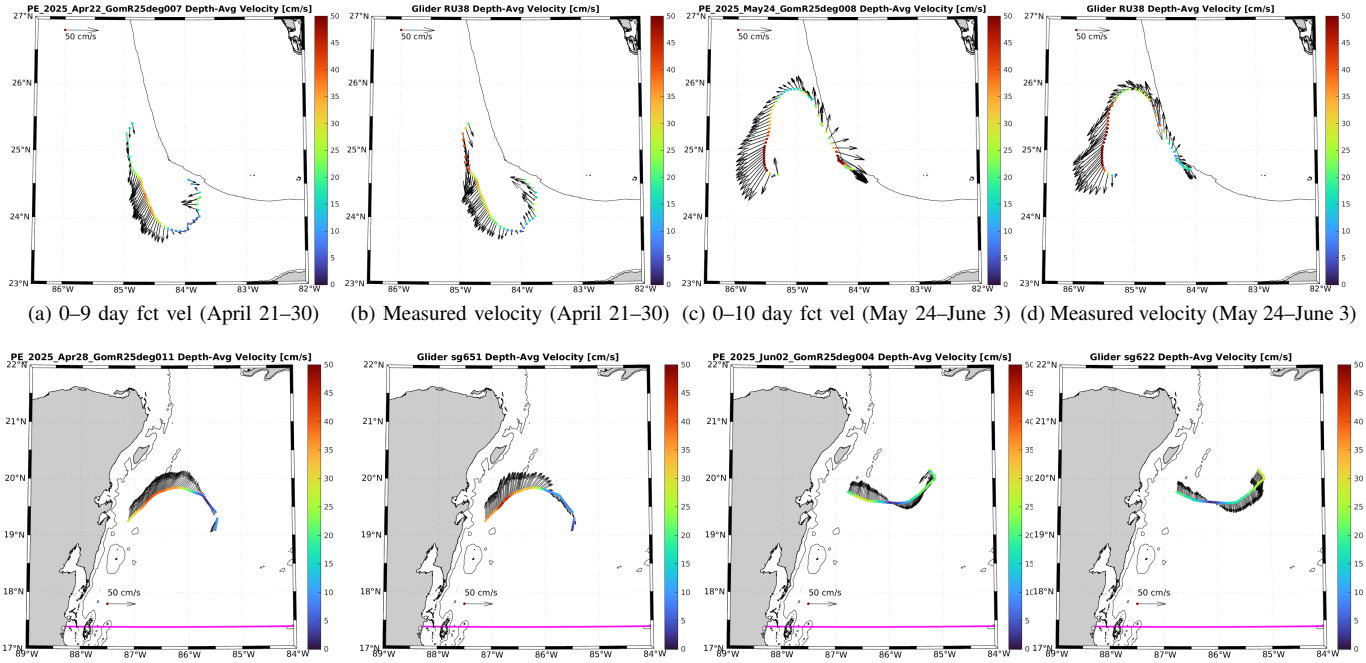

(a) 0–9 day fct vel (April 21–30) (b) Measured velocity (April 21–30) (c) 0–10 day fct vel (May 24–June 3) (d) Measured velocity (May 24–June 3)

(e) 0–10 day fct vel (April 28–May 8) (f) Measured velocity (April 28–May 8) (g) 0–15 day fct vel (June 2–17) (h) Measured velocity (June 2–17)

Fig. 4: Comparison of 0–1000 m average velocity from MSEAS-PE deterministic forecasts, interpolated to observation locations and times, with the independent depth-averaged velocity measured by gliders (once known). (a,c,e,g) MSEAS-PE forecast velocity magnitude and direction (cm/s); depth-averaged velocities measured by gliders RU38 (b,d), SG651 (f), and SG622 (h).

(a) Target locs. overlaid on 300 m mean T (b) Target locs. overlaid on 300 m T std. dev.

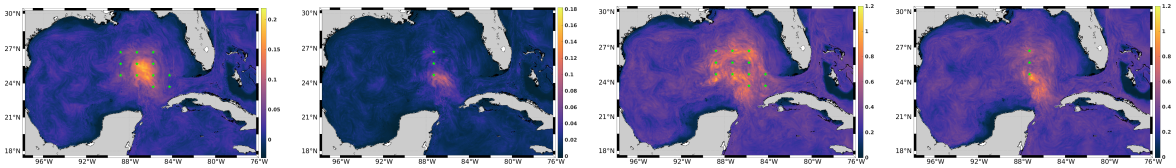

(c) MI, targeting σ_T in whole LC head (d) MI, targeting σ_T in west LC line (e) MI, targeting U+V in whole LC head (f) MI, targeting U+V in west LC line

Fig. 5: MSEAS real-time MI forecast products. Candidate measurements are 0 m, 50 m, 150 m, 300 m and 500 m T and S (together) on April 30. Verification (target) date is May 6; verification depths are 150 m, 300 m, and 500 m, at the locations indicated by green stars. (a,b) Verification (target) locations overlaid on 300 m ensemble mean T (a) and T standard deviation (b). Verification variables are σ_T (c,d), U and V (together) (e,f). We target the whole LC head in (c,e), but only a subset of points along the western edge of the LC in (d,f).

May 9 that are most informative about the LC neck (possible separation region) 10 days later (see Fig. 6a–b). We thus seek to predict the locations of candidate data most informative about either σ_T or U and V on May 19, in the LC neck at 150 m, 300 m, and 500 m (together). We forecast that the deep T/S profiles on May 9 that are most informative: about σ_T on May 19, are north of the neck in the LC head (Fig. 6c); about U and V (together) on May 19, are also in the LC head, but also on the northern flank of the anticyclone in the western Caribbean (Fig. 6d). We also forecast that the deep U/V profiles on May 9 that are most informative: about σ_T on May 19, are in the LC head, not the neck (Fig. 6e); about U/V on May 19, are also mainly in the LC head, but also just south of the Yucatan Strait (Fig. 6f).

VI. Optimal Float Planning and Forecasting

a) Float Deployment Planning and Reachability: On June 5, the GRASE EM-APEX float team planned to deploy floats in two LCFEs and the LC core, and remain within these features. The first float aimed to start in the center of an LCFE then located at the northwest end of the LC and remain in it. The second aimed to start and remain in the Tortugas LCFE, while the third aimed to start and remain in the LC core.

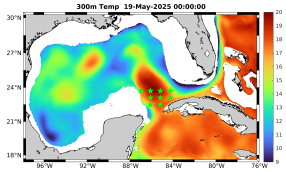

(a) Target locs. overlaid on 300 m mean T

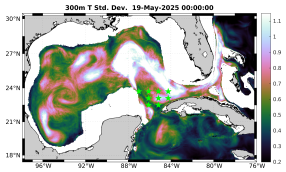

(b) Target locs. overlaid on 300 m T std. dev.

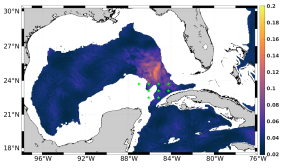

(c) MI: T+S data, targeting σ_T

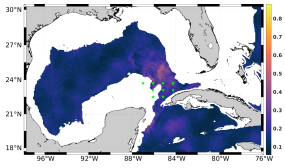

(d) MI: T+S data, targeting U+V

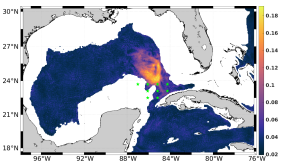

(e) MI: U+V data, targeting σ_T

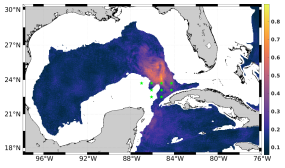

(f) MI: U+V data, targeting U+V

Fig. 6: MSEAS real-time MI forecast products. Candidate measurements are at 1000 m and 1500 m depth (together) on May 9. Verification (target) date is May 19; verification depths are 150 m, 300 m, and 500 m, at the locations in the LC neck indicated by green stars. (a,b) Verification (target) locations overlaid on 300 m ensemble mean T (a) and T standard deviation (b) on May 6. Candidate observation variables are T and S (together) (c,d), and U and V (together) (e,f). Verification variables are σ_T (c,e), and U and V (together) (d,f).

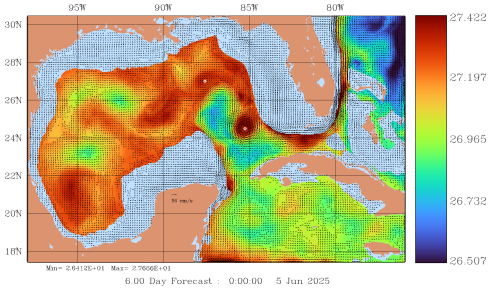

(a) Fct 500 m σ_T field, fct modeled velocity field experienced by the floats, and fct LCFE centers (June 5)

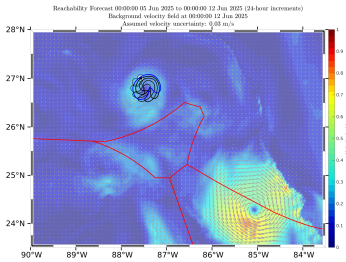

(b) Reachability fct (June 5–12); Northwest LCFE deployment

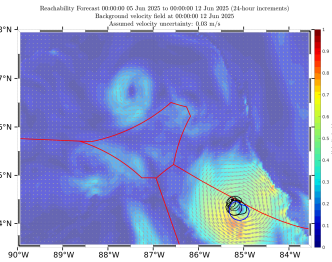

(c) Reachability fct (June 5–12); Tortugas LCFE deployment

Fig. 7: MSEAS float deployment planning products. (a) 6-day MSEAS-PE forecast of LCFE centers (white dots) for June 5; (b) 0–7 day daily reachability forecasts for June 5–12, overlaid on simulated float-experienced velocity field, for a float deployed at the forecast center of the northwest LCFE. (b) As (a), but for a float depoyed in the forecast Tortugas LCFE. Assumed velocity uncertainty is 3 cm/s.

As such, starting from a 6-day MSEAS-PE forecast, we first identified the two LCFE centers based on water mass analyses (T, S, and σ_T) and velocity and vorticity fields at several depths to account for possible titled eddies, filamentation at their edges, and separation into surface/deeper eddies (Fig. 7a, white dots). Next, we constructed the forecast 2D horizontal velocity field experienced by the EM-APEX floats, accounting for their vertical motions: e.g., one up/down profile per day (0 to 1500 m), taking 8.5 hours, and spend the rest of the day parked at 1500 m (actual parking depth differed). Using

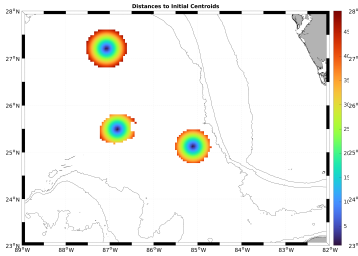

(a) Initial positions (June 6)

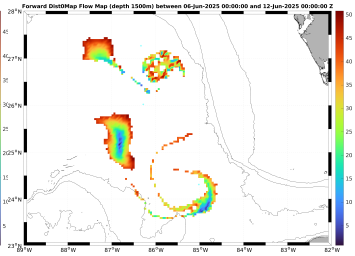

(b) Positions fct for June 12

Fig. 8: MSEAS forecasts of 1500 m, 6-day float flow maps for 3 EM-APEX floats deployed June 6 at the locations colored in blue. (a) Float deployment locations and regions, colored by initial distance from the centroid of the region; (b) Forecast locations of the float regions on June 12.

this float-experienced velocity field, we provided reachability forecasts for the floats, assuming a 3 cm/s horizontal velocity uncertainty over time (Fig. 7b–c). The float starting in the northwest cyclonic LCFE was forecast to remain trapped in the eddy on the northwest flank of the LC, while the float starting in the east LCFE was forecast to move slightly SE but also remain entrained in the eddy.

b) Float Flow maps: Once the floats were deployed on June 6 and their initial positions known, we provided float flow map forecasts of the final location of the material region surrounding the floats' initial positions; the boundaries were selected based on Lagrangian feature analysis (coherent structures, FTLE, etc., see [33]). Fig. 8 shows the initial and 6-day forecast of these regions' locations, colored by initial distance from the centroid of the region on June 6. This highlights how each region is being distorted, especially how its edges can be affected by shear and turbulence. Floats starting in the northern LCFE region on June 6 are forecast to advect eastward along the LC and largely split in two parts by June 11. Even floats from the centroid are strongly sheared and split between two new smaller float-regions. Floats from the Tortugas LCFE region mostly remain coherent and within the

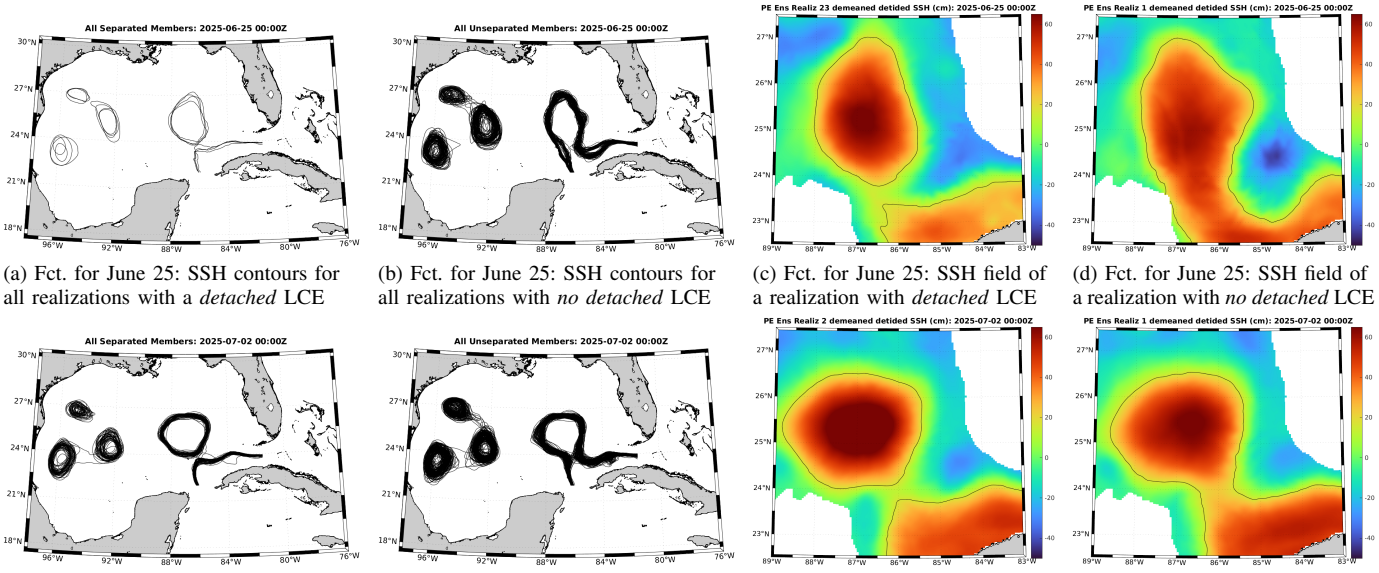

(a) Fct. for June 25: SSH contours for all realizations with a *detached* LCE

(b) Fct. for June 25: SSH contours for all realizations with *no detached* LCE

(c) Fct. for June 25: SSH field of a realization with *detached* LCE

(d) Fct. for June 25: SSH field of a realization with *no detached* LCE

(e) Fct. for July 2: SSH contours for all realizations with a *detached* LCE

(f) Fct. for July 2: SSH contours for all realizations with *no detached* LCE

(g) Fct. for July 2: SSH field of a realization with *detached* LCE

(h) Fct. for July 2: SSH field of a realization with *no detached* LCE

Fig. 9: MSEAS 5-day ensemble probabilistic forecasts of the LC and LCE locations and SSH fields for June 25 (top row, 100 ensemble members) and July 2 (bottom row, 195 ensemble members): (a,b,e,f) De-tided, de-meaned 17 cm SSH contours, restricted to areas of the Gulf proper with bathymetry deeper than 200 m, of all realizations showing an LCE separation on the forecast date (a,e) and no separation (b,f); (c,d,g,h) De-tided, de-meaned SSH fields, restricted to areas of the Gulf proper with bathymetry deeper than 200 m, of one selected member showing an LCE separation (c,g) and no separation (d,h). The 17 cm SSH contour is shown in black.

region they started until June 9. Later, float locations mostly on the edges are strained into filaments forming from the LCFE edges. Finally, floats starting in the LC core are forecast to remain within the LC but advected to the southeast with some distortion but less filamentation than the other float-regions.

VII. Probabilistic Loop Current Eddy Forecasting

When some forecasts and data suggested the possibility of an LCE separation event, we used our MSEAS probabilistic forecasts to assess the likelihood of such a separation [53]. To obtain probabilities, we clustered our large ensemble forecasts [62, 63] into two groups of realizations: those that predicted separation and those that did not. To define eddies, we used the 17 cm de-tided SSH contour in the deeper Gulf [4]. Hence, for reach realizations, we de-tide the SSH field and de-mean it over the region north of 22°N, west of 81.5°W, and deeper than 200 m (i.e., considering only the deep waters in the Gulf). We then extract the 17 cm contours of the resulting field, highlighting the locations of the LC and LCEs. To identify possible new LCE separation, we eliminate eddy remnants in the western Gulf by restricting to the region between 22.5°N and 27.5°N and between 89°W and 83°W. If a closed contour with an arclength of at least 200 km is fully contained in this region, this can indicate LCE detachment. We finally examine these realizations and count the number of LCE detachments.

Fig. 9 illustrates two such clustering of our real-time ensemble forecasts: both are 5-day forecasts, one is for June 25 (100 members) and the other for July 2 (195 members). We find that 96% of the ensemble realizations predict no LCE detachment on June 25 (Fig. 9b), while 73.8% of the realizations predict no detachment on July 2. In other words, the forecast for July 2 suggested, at best, a 24% chance of a partial detachment of an LCE (named Feldman) from the LC. This was the highest likelihood of detachment that we predicted within May, June and July, 2025. As shown on Fig. 9e, we find that among the closed 17 cm SSH contours, many remain very close to the LC contour itself and cannot ensure full separation. These low LCE detachment probabilities are indeed overstated: for example, many of the realizations that indicate LCE detachment using the 17 cm SSH-based metric do not show separation in their 300 m and 500 m velocity fields (not shown).

VIII. Optimal Glider Recovery

We issued special reachability and path planning forecasts to assist in the recovery of gliders at the end of their missions.

a) Recovery of Glider RU38: After two months at sea, in mid-June, glider RU38 was sampling the Tortugas LCFE with a low battery, and needed to reach target point (25°41.1′N, 84°41.3′W) in low currents away from the LC for recovery. Using the glider position on June 18 14:05Z, we predicted the time-optimal path and headings shown in Fig. 10; the path exploits currents, spiraling around the eddy to its target point. The glider followed our optimal path ideas, with a propulsion speed of about 20 cm/s to conserve battery, counter-clockwise around the LCFE, tracing out the track shown in Fig. 10c (similar to Fig. 10b). It reached the target point in approximately 10 days, as predicted by our forecast. The glider was successfully recovered in early July.

b) Recovery of Glider Howdy: Similarly, in mid-June, glider Howdy, after sampling the Tortugas LCFE, was entering Gulf Stream currents in the Florida Strait. The plan was to recover the glider near Key West. Starting from its position on

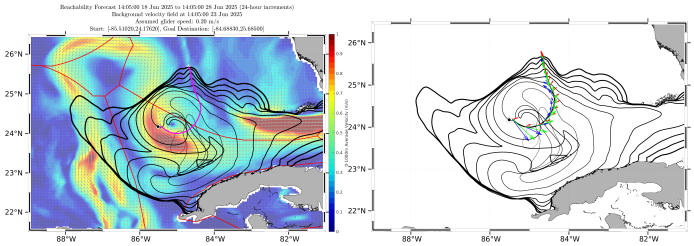

(a) Time-optimal path: June 18–28 (b) Optimal headings: June 18–28

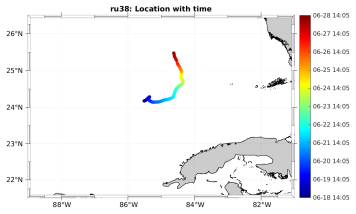

(c) Actual track: June 18–28

Fig. 10: MSEAS forecast products issued June 18 for glider RU38 recovery. Assumed glider speed is 20 cm/s. (a) Daily reachability fronts and forecast time-optimal path for June 18–28 overlaid on mid-time 0–1000 m average velocity; (b) optimal path and controls, with forecast current (blue), optimal vehicle propulsion (red), and net total velocity (green) vectors, overlaid on reachability fronts; (c) Actual track of RU38 from June 18 to June 28.

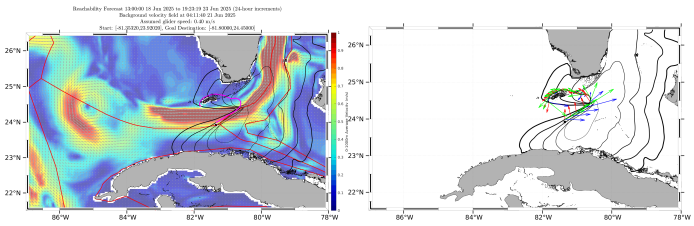

(a) Time-optimal path: June 18–23 (b) Optimal headings: June 18–23

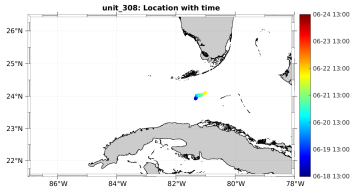

(c) Actual track: June 18–23

Fig. 11: MSEAS forecast products issued June 18 for glider Howdy recovery. Assumed glider speed is 40 cm/s. (a) Daily reachability fronts and forecast time-optimal path for June 18–23 overlaid on mid-time 0–1000 m average velocity; (b) optimal path and controls, with forecast current (blue), optimal vehicle propulsion (red), and net total velocity (green) vectors, overlaid on reachability fronts; (c) Actual track of Howdy from June 18 to June 23.

June 18 13:00Z, we predicted the time-optimal path and headings shown in Fig. 11, assuming a target point just south of Key West. This fastest path follows a circuitous route around the Keys, passing between Upper and Lower Matecumbe Key, exploiting the quiescent waters north of the Keys and rounding Key West to the target (Fig. 11a). The glider was first piloted northeastward (as the first 2 days of the forecast), but was then recovered early off Marathon Key on June 26.

IX. Conclusions

In this paper, we showcased some of our real-time forecast products for the GRASE experiment from April to September, 2025, resulting from the use of our MSEAS systems. We provided deterministic and large-ensemble 5-to-20-day forecasts that showed predictive skill when compared to independent data. We applied our path planning to provide probabilistic reachability products for gliders, and showed that actual tracks remain within our forecast reachability fronts and that headings could be followed by gliders. We issued MI forecasts for adaptive sampling for multiple sensing platforms, considering varied candidate measurement variables and depths for different types, locations, and times of verification variables. We successfully assisted the GRASE float deployment and planned and forecast future positions of floats and surrounding waters. We issued probabilistic forecasts of LCE separation, showing that an LCE detachment in June/early July was very unlikely. Lastly, we successfully assisted the recovery of gliders, guiding multiple gliders towards designated recovery points in minimal time, conserving battery. These results can inform future GoM field campaigns, and offer valuable insights for stakeholders in the region.

Acknowledgments

We thank all members of the MIT-MSEAS group and all of our UGOS colleagues. We also thank the HYCOM Consortium and Mercator Ocean for their ocean model fields, and NCEP for their atmospheric forecasts. We acknowledge support from the Gulf Research Program of the National Academies of Sciences, Engineering, and Medicine under award number 2000013149. The content is solely the responsibility of the authors and does not necessarily represent the official views of the Gulf Research Program or the National Academies of Sciences, Engineering, and Medicine.

References

[1] The National Academy of Sciences, "Understanding Gulf ocean systems," 2018. [Online]. Available: https://www.nationalacademies.org/gulf/fellowships-and-grants/understanding-gulf-ocean-systems

[2] S. F. DiMarco, W. D. Nowlin, and R. Reid, "A statistical description of the velocity fields from upper ocean drifters in the Gulf of Mexico," *Geophys. Monog.-AGU*, vol. 161, p. 101, 2005.

[3] A. K. Nickerson, R. H. Weisberg, and Y. Liu, "On the evolution of the Gulf of Mexico loop current through its penetrative, ring shedding and retracted states," *Adv. Space Res.*, vol. 69, no. 11, pp. 4058–4077, 2022.

[4] D. S. Dukhovskoy, R. R. Leben, E. P. Chassignet, C. A. Hall, S. L. Morey, and R. Nedbor-Gross, "Characterization of

the uncertainty of loop current metrics using a multidecadal numerical simulation and altimeter observations," *Deep Sea Res. Part I*, vol. 100, pp. 140–158, 2015.

[5] D. S. Dukhovskoy, E. P. Chassignet, A. Bozec, and S. L. Morey, "Assessment of predictability of the Loop Current in the Gulf of Mexico from observing system experiments and observing system simulation experiments," *Front. Mar. Sci.*, vol. 10, 2023.

[6] R. J. Brokaw, B. Subrahmanyam, and S. L. Morey, "Loop current and eddy-driven salinity variability in the Gulf of Mexico," *Geophys. Res. Lett.*, vol. 46, no. 11, pp. 5978–5986, 2019.

[7] S. L. Morey, R. He, E. P. Chassignet, and J. Sheinbaum, "Editorial: Understanding and predicting the Gulf of Mexico ocean dynamics," *Front. Mar. Sci.*, vol. 11, 2024.

[8] M. Le Hénaff, R. Domingues, G. Halliwell, J. A. Zhang, H.-S. Kim, M. Aristizabal, T. Miles, S. Glenn, and G. Goni, "The role of the Gulf of Mexico ocean conditions in the intensification of Hurricane Michael (2018)," *J. Geophys. Res. Oceans*, vol. 126, no. 5, p. e2020JC016969, 2021.

[9] L. Hiron, B. J. de la Cruz, and L. K. Shay, "Evidence of Loop Current Frontal Eddy intensification through local linear and nonlinear interactions with the Loop Current," *J. Geophys. Res. Oceans*, vol. 125, no. 4, p. e2019JC015533, 2020.

[10] L. Hiron, P. Miron, L. K. Shay, W. E. Johns, E. P. Chassignet, and A. Bozec, "Lagrangian coherence and source of water of Loop Current Frontal eddies in the Gulf of Mexico," *Prog. Oceanogr.*, vol. 208, p. 102876, 2022.

[11] S. F. DiMarco, S. M. Glenn, B. Jaimes de la Cruz, R. M. Jiménez, A. H. Knap, Y. Liu, B. Magnell, S. Mahmud, T. N. Miles, E. Pallas-Sanz, R. Ramos, D. A. Salas de León, L. K. Shay, M. Smith, M. Tenreiro, and R. H. Weisberg, "Applications of adaptive sampling strategies of autonomous vehicles, drifters, floats, and HF-Radar, to improve Loop Current system dynamics forecasts in the deepwater Gulf of Mexico," in *Offshore Tech. Conf.*, Houston, May 2023, p. D031S035R005.

[12] K. A. Donohue, D. R. Watts, P. Hamilton, R. Leben, M. Kennelly, and A. Lugo-Fernández, "Gulf of Mexico Loop Current path variability," *Dynam. Atmos. Oceans*, vol. 76, pp. 174–194, 2016, the Loop Current Dynamics Experiment.

[13] K. A. Donohue, D. R. Watts, P. Hamilton, R. Leben, and M. Kennelly, "Loop current eddy formation and baroclinic instability," *Dynam. Atmos. Oceans*, vol. 76, pp. 195–216, 2016, the Loop Current Dynamics Experiment.

[14] T. Meunier, P. Pérez Brunius, J. Rodríguez Outerelo, P. García Carrillo, A. Ronquillo, H. Furey, A. Ramsey, and A. Bower, "A deep water dispersion experiment in the Gulf of Mexico," *J. Geophys. Res. Oceans*, vol. 126, no. 10, p. e2021JC017375, 2021.

[15] J. Jouanno, J. Ochoa, E. Pallàs-Sanz, J. Sheinbaum, F. Andrade-Canto, J. Candela, and J.-M. Molines, "Loop current frontal eddies: Formation along the campeche bank and impact of coastally trapped waves," *J. Phys. Oceanogr.*, vol. 46, no. 11, pp. 3339–3363, 2016.

[16] J. Candela, J. Ochoa, J. Sheinbaum, M. López, P. Pérez-Brunius, M. Tenreiro, E. Pallàs-Sanz, G. Athié, and L. Arriaza-Oliveros, "The flow through the Gulf of Mexico," *J. Phys. Oceanogr.*, vol. 49, no. 6, pp. 1381–1401, 2019.

[17] A. C. Poje, T. M. Özgökmen, B. L. Lipphardt, B. K. Haus, E. H. Ryan, A. C. Haza, G. A. Jacobs, A. J. H. M. Reniers, M. J. Olascoaga, G. Novelli, A. Griffa, F. J. Beron-Vera, S. S. Chen, E. Coelho, P. J. Hogan, A. D. Kirwan, H. S. Huntley, and A. J. Mariano, "Submesoscale dispersion in the vicinity of the Deepwater Horizon spill," *Proc. Natl. Acad. Sci.*, vol. 111, no. 35, pp. 12 693–12 698, 2014.

[18] T. M. Özgökmen, E. P. Chassignet, C. N. Dawson, D. Dukhovskoy, G. Jacobs, J. Ledwell, and O. Garcia-Pineda, "Over what area did the oil and gas spread during the 2010 Deepwater Horizon oil spill?" *Oceanography*, vol. 29, no. 3, pp. 96–107, 2016.

[19] S. F. DiMarco *et al.*, "Results of the Mini-Adaptive Sampling Test Run (MASTR) experiment: Autonomous vehicles, drifters, floats, ROCIS, and HF-Radar, to improve loop current system dynamics and forecasts in the deepwater Gulf of México," in *Offshore Tech. Conf.*, Houston, 2024, pp. OTC–35 072–MS.

[20] P. F. J. Lermusiaux, P. J. Haley, Jr., C. Mirabito, E. M. Mule, S. F. DiMarco, A. Dancer, X. Ge, A. H. Knap, Y. Liu, S. Mahmud, U. C. Nwankwo, S. Glenn, T. N. Miles, D. Aragon, K. Coleman, M. Smith, M. Leber, R. Ramos, J. Storie, G. Stuart, J. Marble, P. Barros, E. P. Chassignet, A. Bower, H. H. Furey, B. Jaimes de la Cruz, L. K. Shay, M. Tenreiro, E. Pallàs Sanz, J. Sheinbaum, P. Pérez Brunius, D. Wilson, J. van Smirren, R. Monreal Jiménez, D. A. Salas de León, V. K. Contreras Tereza, M. Feldman, and M. Khadka, "Real-time ocean probabilistic forecasts, reachability analysis, and adaptive sampling in the Gulf of Mexico," in *Oceans*. Halifax: IEEE, Sep. 2024, pp. 1–10.

[21] M. Larranaga, J. Jouanno, E. P. Chassignet *et al.*, "The role of cyclonic eddies in the detachment and separation of loop current eddies," *J. Geophys. Res.*, 2025.

[22] P. G. Thoppil, C. D. Rowley, P. J. Hogan, and J. Stear, "Evaluating the performance of an ensemble forecast system in predicting Loop Current Eddy separation in the Gulf of Mexico," *Prog. Oceanogr.*, vol. 237, p. 103529, 2025.

[23] L. Hiron, O. Zavala-Romero, E. P. Chassignet, P. Miron, and B. Subrahmanyam, "Identifying and predicting the Lagrangian coherence of eddies in the Gulf of Mexico using machine learning and satellite observations," *J. Geophys. Res. ML Comput.*, vol. 2, no. 2, p. e2025JH000620, 2025.

[24] T. Meunier, E. P. Sanz, M. Tenreiro, J. Ochoa, A. Ruiz Angulo, and C. Buckingham, "Observations of layering under a warm-core ring in the Gulf of Mexico," *J. Phys. Oceanogr.*, vol. 49, no. 12, pp. 3145–3162, 2019.

[25] P. J. Haley, Jr. and P. F. J. Lermusiaux, "Multiscale two-way embedding schemes for free-surface primitive equations in the "Multidisciplinary Simulation, Estimation and Assimilation System"," *Ocean Dynam.*, vol. 60, no. 6, pp. 1497–1537, Dec. 2010.

[26] P. J. Haley, Jr., A. Agarwal, and P. F. J. Lermusiaux, "Optimizing velocities and transports for complex coastal regions and archipelagos," *Ocean Model.*, vol. 89, pp. 1–28, May 2015.

[27] P. J. Haley, Jr., C. Mirabito, M. Doshi, and P. F. J. Lermusiaux, "Ensemble forecasting for the Gulf of Mexico Loop Current region," in *Oceans*. Biloxi, MS: IEEE, Sep. 2023.

[28] MSEAS MASTR Ex., "MASTR Real-time Gulf of Mexico Sea Experiment 2024: Gulf of Mexico – February–April, 2024," Apr. 2024. [Online]. Available: http://mseas.mit.edu/Sea_exercises/GOFFISH/MASTR/

[29] P. F. J. Lermusiaux, P. J. Haley, Jr., S. Jana, A. Gupta, C. S. Kulkarni, C. Mirabito, W. H. Ali, D. N. Subramani, A. Dutt, J. Lin, A. Shcherbina, C. Lee, and A. Gangopadhyay, "Optimal planning and sampling predictions for autonomous and Lagrangian platforms and sensors in the northern Arabian Sea," *Oceanography*, vol. 30, no. 2, pp. 172–185, Jun. 2017.

[30] P. F. J. Lermusiaux, D. N. Subramani, J. Lin, C. S. Kulkarni, A. Gupta, A. Dutt, T. Lolla, P. J. Haley, Jr., W. H. Ali, C. Mirabito, and S. Jana, "A future for intelligent autonomous ocean observing systems," *J. Mar. Res.*, vol. 75, no. 6, pp. 765–813, Nov. 2017, the Sea. Volume 17, The Science of Ocean Prediction, Part 2.

[31] C. S. Kulkarni and P. F. J. Lermusiaux, "Advection without compounding errors through flow map composition," *J. Comput. Phys.*, vol. 398, p. 108859, Dec. 2019.

[32] P. F. J. Lermusiaux, M. Doshi, C. S. Kulkarni, A. Gupta, P. J. Haley, Jr., C. Mirabito, F. Trotta, S. J. Levang, G. R. Flierl,

J. Marshall, T. Peacock, and C. Noble, "Plastic pollution in the coastal oceans: Characterization and modeling," in *Oceans 2019*. IEEE, Oct. 2019, pp. 1–10.

[33] P. F. J. Lermusiaux, P. J. Haley, Jr., and C. Mirabito, "Lagrangian flow map analysis of ocean dynamics and material transports," in *Oceans*. Chicago: IEEE, Sep. 2025, in press.

[34] E. M. Mule, P. J. Haley, C. Mirabito, S. F. DiMarco, S. Mahmud, A. Dancer, X. Ge, A. H. Knap, Y. Liu, U. C. Nwankwo, S. Glenn, T. N. Miles, D. Aragon, K. Coleman, M. Smith, M. Leber, R. Ramos, J. Storie, G. Stuart, J. Marble, P. Barros, E. P. Chassignet, A. Bower, H. H. Furey, B. Jaimes de la Cruz, L. K. Shay, M. Tenreiro, E. Pallàs Sanz, J. Sheinbaum, P. Pérez Brunius, D. Wilson, J. van Smirren, R. Monreal Jiménez, D. A. Salas de León, V. K. Contreras Tereza, M. Feldman, M. Khadka, and P. F. J. Lermusiaux, "Real-time probabilistic reachability forecasting for gliders in the Gulf of Mexico," in *Oceans*. Halifax: IEEE, Sep. 2024, pp. 1–10.

[35] P. F. J. Lermusiaux and A. R. Robinson, "Data assimilation via Error Subspace Statistical Estimation, part I: Theory and schemes," *Mon. Weather Rev.*, vol. 127, no. 7, pp. 1385–1407, 1999.

[36] P. F. J. Lermusiaux, "Data assimilation via Error Subspace Statistical Estimation, part II: Mid-Atlantic Bight shelfbreak front simulations, and ESSE validation," *Mon. Weather Rev.*, vol. 127, no. 7, pp. 1408–1432, Jul. 1999.

[37] P. F. J. Lermusiaux, P. J. Haley, W. G. Leslie, A. Agarwal, O. Logutov, and L. J. Burton, "Multiscale physical and biological dynamics in the Philippine Archipelago: Predictions and processes," *Oceanography*, vol. 24, no. 1, pp. 70–89, 2011.

[38] P. F. J. Lermusiaux, C. Mirabito, P. J. Haley, Jr., W. H. Ali, A. Gupta, S. Jana, E. Dorfman, A. Laferriere, A. Kofford, G. Shepard, M. Goldsmith, K. Heaney, E. Coelho, J. Boyle, J. Murray, L. Freitag, and A. Morozov, "Real-time probabilistic coupled ocean physics-acoustics forecasting and data assimilation for underwater GPS," in *Oceans*. IEEE, 2020, pp. 1–9.

[39] W. G. Leslie, A. R. Robinson, P. J. Haley, Jr, O. Logutov, P. A. Moreno, P. F. J. Lermusiaux, and E. Coelho, "Verification and training of real-time forecasting of multi-scale ocean dynamics for maritime rapid environmental assessment," *J. Marine Syst.*, vol. 69, no. 1, pp. 3–16, 2008.

[40] P. J. Haley, Jr., P. F. J. Lermusiaux, A. R. Robinson, W. G. Leslie, O. Logoutov, G. Cossarini, X. S. Liang, P. Moreno, S. R. Ramp, J. D. Doyle, J. Bellingham, F. Chavez, and S. Johnston, "Forecasting and reanalysis in the Monterey Bay/California Current region for the Autonomous Ocean Sampling Network-II experiment," *Deep Sea Res. Part II*, vol. 56, no. 3–5, pp. 127–148, Feb. 2009.

[41] D. N. Subramani, P. J. Haley, Jr., and P. F. J. Lermusiaux, "Energy-optimal path planning in the coastal ocean," *J. Geophys. Res. Oceans*, vol. 122, pp. 3981–4003, 2017.

[42] C. S. Kulkarni, P. J. Haley, Jr., P. F. J. Lermusiaux, A. Dutt, A. Gupta, C. Mirabito, D. N. Subramani, S. Jana, W. H. Ali, T. Peacock, C. M. Royo, A. Rzeznik, and R. Supekar, "Real-time sediment plume modeling in the Southern California Bight," in *Oceans 2018*. Charleston, SC: IEEE, Oct. 2018.

[43] A. Gupta, P. J. Haley, D. N. Subramani, and P. F. J. Lermusiaux, "Fish modeling and Bayesian learning for the Lakshadweep Islands," in *Oceans 2019*. IEEE, Oct. 2019, pp. 1–10.

[44] P. F. J. Lermusiaux, D. G. M. Anderson, and C. J. Lozano, "On the mapping of multivariate geophysical fields: Error and variability subspace estimates," *Quart. J. Roy. Meteorol. Soc.*, vol. 126, no. 565, pp. 1387–1429, 2000.

[45] P. F. J. Lermusiaux, "On the mapping of multivariate geophysical fields: Sensitivities to size, scales, and dynamics," *J. Atmos. Ocean. Tech.*, vol. 19, no. 10, pp. 1602–1637, 2002.

[46] O. G. Logutov and P. F. J. Lermusiaux, "Inverse barotropic tidal estimation for regional ocean applications," *Ocean Model.*, vol. 25, no. 1–2, pp. 17–34, 2008.

[47] A. Agarwal and P. F. J. Lermusiaux, "Statistical field estimation for complex coastal regions and archipelagos," *Ocean Model.*, vol. 40, no. 2, pp. 164–189, 2011.

[48] P. F. J. Lermusiaux, "Evolving the subspace of the three-dimensional multiscale ocean variability: Massachusetts Bay," *J. Marine Syst.*, vol. 29, no. 1, pp. 385–422, 2001.

[49] P. F. J. Lermusiaux, "Uncertainty estimation and prediction for interdisciplinary ocean dynamics," *J. Comput. Phys.*, vol. 217, no. 1, pp. 176–199, 2006.

[50] P. F. J. Lermusiaux, T. Lolla, P. J. Haley, Jr., K. Yigit, M. P. Ueckermann, T. Sondergaard, and W. G. Leslie, "Science of autonomy: Time-optimal path planning and adaptive sampling for swarms of ocean vehicles," in *Springer Handbook of Ocean Engineering*, T. Curtin, Ed. Springer, 2016, ch. 21, pp. 481–498.

[51] P. F. J. Lermusiaux, P. J. Haley, Jr, and N. K. Yilmaz, "Environmental prediction, path planning and adaptive sampling: Sensing and modeling for efficient ocean monitoring, management and pollution control," *Sea Technol.*, vol. 48, no. 9, pp. 35–38, 2007.

[52] P. F. J. Lermusiaux, "Adaptive modeling, adaptive data assimilation and adaptive sampling," *Physica D*, vol. 230, no. 1, pp. 172–196, 2007.

[53] MSEAS GRASE Ex., "GRand Adaptive Sampling Experiment (GRASE) 2025: Gulf of Mexico — April–September 2025," Apr. 2025. [Online]. Available: http://mseas.mit.edu/Sea_exercises/GOFFISH/GRASE/

[54] P. F. J. Lermusiaux, A. J. Miller, and N. Pinardi, "Special issue of Dynamics of Atmospheres and Oceans in honor of Prof. A. R. Robinson," *Dynam. Atmos. Oceans*, vol. 52, no. 1–2, pp. 1–3, Sep. 2011, Editorial.

[55] P. F. J. Lermusiaux, P. Malanotte-Rizzoli, D. Stammer, J. Carton, J. Cummings, and A. M. Moore, "Progress and prospects of U.S. data assimilation in ocean research," *Oceanography*, vol. 19, no. 1, pp. 172–183, 2006.

[56] C. S. Kulkarni and P. F. J. Lermusiaux, "Three-dimensional time-optimal path planning in the ocean," *Ocean Model.*, vol. 152, Aug. 2020.

[57] T. Lolla, P. F. J. Lermusiaux, M. P. Ueckermann, and P. J. Haley, Jr., "Time-optimal path planning in dynamic flows using level set equations: Theory and schemes," *Ocean Dynam.*, vol. 64, no. 10, pp. 1373–1397, 2014.

[58] T. Lolla, P. J. Haley, Jr., and P. F. J. Lermusiaux, "Path planning in multiscale ocean flows: Coordination and dynamic obstacles," *Ocean Model.*, vol. 94, pp. 46–66, 2015.

[59] D. N. Subramani, Q. J. Wei, and P. F. J. Lermusiaux, "Stochastic time-optimal path-planning in uncertain, strong, and dynamic flows," *Comput. Meth. Appl. Mech. Engrg.*, vol. 333, pp. 218–237, 2018.

[60] D. N. Subramani and P. F. J. Lermusiaux, "Risk-optimal path planning in stochastic dynamic environments," *Comput. Meth. Appl. Mech. Engrg.*, vol. 353, pp. 391–415, Aug. 2019.

[61] M. Doshi, M. Bhabra, M. Wiggert, C. J. Tomlin, and P. F. J. Lermusiaux, "Hamilton–Jacobi multi-time reachability," in *IEEE 61st CDC*, Cuncún, Dec. 2022, pp. 2443–2450.

[62] M. M. Swezey, "Ocean acoustic uncertainty for submarine applications," Master's thesis, MIT, MechE, Cambridge, MA, Jun. 2016.

[63] A. Dutt, D. N. Subramani, C. S. Kulkarni, and P. F. J. Lermusiaux, "Clustering of massive ensemble of vehicle trajectories in strong, dynamic and uncertain ocean flows," in *Oceans*. Charleston, SC: IEEE, Oct. 2018.